Special Issue: JMES 60th Anniversary Special Issue

Corresponding Author:

Rongjie Kang, Key Laboratory of Mechanism Theory and Equipment Design of the Ministry of Education, International Centre for Advanced Mechanisms and Robotics, Tianjin University, Tianjin 300354, China

Email: rjkang@tju.edu.cn

Task Space Based Orientability Analysis and Optimization of a Wire-Driven Continuum Robot

Cong Wang[1], Shineng Geng[1], David T Branson[2], Chenghao Yang[1,3], Jian S. Dai[1,4] and Rongjie Kang[1,*]

[1]Key Laboratory of Mechanism Theory and Equipment Design of the Ministry of Education, International Centre for Advanced Mechanisms and Robotics, Tianjin University, Tianjin 300354, China

[2]Faculty of Engineering, University of Nottingham, Nottingham NG7 2RD, U.K.

[3]School of Mechanical Engineering, Tianjin Polytechnic University, Tianjin 300160, China

[4]Centre for Robotics Research, School of Physical Sciences and Engineering, King's College, London WC2R 2LS, U.K.

Abstract

Compared to traditional rigid robots, continuum robots have intrinsic compliance and therefore behave dexterously when performing tasks in restricted environments. Although there have been many researches on the design and application of continuum robots, a theoretical investigation of their dexterity is still lacking. In this paper, a two-joint wire-driven continuum robot is utilized to demonstrate dexterity by introducing the concept of orientability taking into account two indices, the accessible ratio and angle of the robot, when its tip reaches a certain task space inside the workspace. Based on the kinematic model, the accessible ratio and angle of the continuum robot are calculated using the Monte-Carlo method. From this, the influence of individual joint lengths on the proposed orientability indices and the optimal joint length are then investigated via an improved particle swarm optimization (PSO) algorithm. Finally, the presented methods were validated through experiments showing that the use of optimal joint length can increase the accessible ratio and reduce the minimum accessible angle by more than 10° in the task space.

Keywords

Continuum robots, kinematic model, dexterity, orientability, structural optimization

1. Introduction

In recent years, continuum robots mimicking biological structures such as octopus tentacles and elephant trunks have gained increasing attention due to their unique structural advantages of inherent compliance and adaptability. This enables them to be suitable for operations in narrow, complex and unconstructed environments such as detection, rescue, and medical fields[1].

So far, there have been many related researches on the design and implementation of continuum robots. Walker et al.[2-4] developed a series of continuum robots, such as the Air-OCTOR driven by a mixture of wires and air pressure. Xu et al.[5] exploited a continuum robot for minimally invasive surgery in the throat, using multiple super-elastic wires for actuation. Okamura et al.[6] proposed a concentric tube continuum robot with 3-D printed method, which can be used in patient-specific applications. Kang et al.[7-9] presented several continuum robots driven by pneumatic muscle actuators and wires for underwater and restricted environments. Kim et al.[10] designed a flexible spring-based continuum robot composed of an inter-connected inner spring and an outer spring to meet the demand for motions in three dimensions. The above-mentioned continuum robots show higher dexterity in manipulation than traditional rigid robots, but few works were concerned with the quantitative evaluation and analysis of the dexterity for continuum robots. To do this, a kinematic model of continuum robot is required.

There have been a lot of attempts to establish kinematic models for continuum robots. Walker et al.[11] introduced a modified D-H method for the kinematic model of continuum robots. Camarillo et al.[12] came up with a novel linear method to derive the kinematic model for a wire-driven continuum robot. Webster et al.[13] presented a continuum robot composed of telescoping, concentric, precurved superelastic tubes, whose kinematic model was obtained by beam mechanics. Based on the above works, workspace of continuum robots has been further studied. Yuan et al.[14] carried on workspace analysis of wire-driven continuum manipulators taking into account the wire tension, payload and gravity. Burgner-Kahrs et al.[15] described a method for calculating the volume of workspace for a concentric tube continuum robot. Kang et al.[16] proposed a wire-driven continuum robot and analyzed its workspace based on mechanical interference identification. Although these works gave methodologies to calculate the workspace of continuum robots based on kinematic models, the definition of dexterity and how to use the dexterity to optimize the structural design of continuum robots are still lacking.

Within the scope of rigid robots, the following two types of indices were generally used to characterize their dexterity: the manipulability[17-19] evaluating the stability of the tip position of a robot with respect to small changes of displacement in actuators, and the orientability[20-22] representing the ability of a robot to reach a specific position or space in different orientations. Inspired by these methods, Kang et al.[23] used the condition number of the Jacobian matrix to analyze the manipulability of a continuum robot, and Wu et al.[24] investigated the orientability of a continuum robot by identifying an accessible region (also referred to as service region in some papers[22]) where the robot tip can reach through different body configurations. It was found that, the orientability describing dexterity in a geometric way is more straightforward than the manipulability using an algebraic way, thus, it is utilized in this paper for dexterity analysis. To normalize the orientability of a continuum robot with respect to a given task space, an index named accessible ratio is presented in our study meaning the area ratio of the accessible region to the surface of the task space. Unlike the previous work[24] that identified the accessible region by only counting the number of possible configurations, this paper proposes a new index, accessible angle, to further characterize the perpendicularity of the robot tip to the surface of the task space, and therefore provides a more comprehensive evaluation of orientability. Moreover, the indices of accessible ratio and angle are integrated into an objective function to optimize the structure of a wire-driven continuum robot.

The main contributions of this paper are: the orientability indices including the accessible ratio and angle are presented; the individual joint lengths of a continuum robot are then optimized to figure out their influence on the accessible ratio and angle within a specific task pace. This work provides a useful guidance for the structural design of wire-driven continuum robots, and can be applied to designs of other continuum robots as long as they have serially connected bending joints.

This paper is organized as follows. Section 2 introduces the construction of a kinematic model for the continuum robot. Then in Section 3, the orientability of the continuum robot and the influence of the individual joint lengths on it are analyzed in detail. Subsequently, the individual joint lengths of the continuum robot are optimized by comprehensively considering the orientability indices in Section 4. Results are then experimentally validated in Section 5, and Section 6 summarizes the paper.

2. Structure and Kinematic Model of the Robot

2.1 Structure of the robot

Up to now, the classification of continuum robots according to the actuation methods can be divided into wire-driven mechanisms, pneumatic muscles, SMA, etc[1]. Among them, the wire-driven mechanisms are the most widely used due to their relatively simple structure and high precision. In this paper, a wire-driven continuum

robot is used to carry out orientability analysis and structural optimization, as shown in Fig. 1. The robot consists of two modular joints, each of which contains a central backbone, three driving wires and multiple constraint disks. The backbone runs through two joints and functions as a support to the body of the robot. The constraint disks are fixed to the backbone with an equally spaced distance. The driving wires are fixed to the top constraint disk of the corresponding joint, and pass through the holes arranged 120° apart in the constraint disks. Because the length of the backbone is constant, bending motion of the robot can be achieved by changing the length of the driving wires. The backbone and the driving wires are made of superelastic NiTi alloy to ensure the compliance of the continuum robot while the driving wires can take both thrust and tensile forces for a bidirectional control. The robot can be easily modularized to desired length by adding or removing the joints and constraint disks.

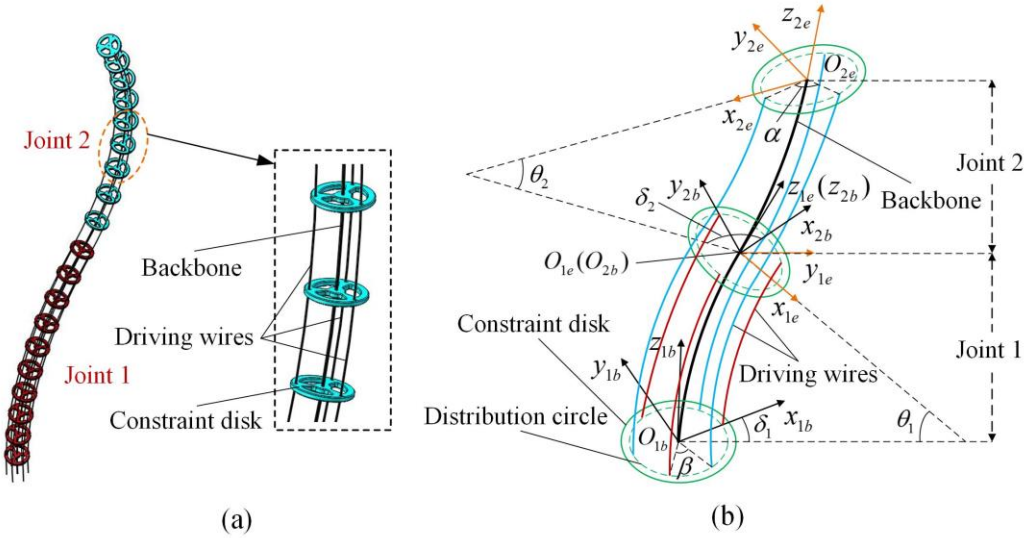

Fig. 1 A two-joint wire-driven continuum robot: (a) Three-dimensional model; (b) Geometric model (to make the figure clear, the constraint disks in the middle of each joint are not drawn).

2.2 Parameter description

In this section, we define the geometrical parameters of the continuum robot. As shown in Fig. 1, two coordinate systems O_{mb} (x_{mb}, y_{mb}, z_{mb}) and O_{me} (x_{me}, y_{me}, z_{me}) are established in joint m (m = 1, 2), respectively:

1) O_{mb} (x_{mb}, y_{mb}, z_{mb}) is the base coordinate system fixed on the center of the base of joint m, where the x_{mb} axis passes through the intersection of the first driving wire and the base of joint m.

2) O_{me} (x_{me}, y_{me}, z_{me}) is the end coordinate system of the tip of joint m, where the x_{me} axis is in the bending plane of joint m.

Assuming the bending shape of each joint has constant curvature, three spaces of the continuum robot are described[25]:

1) Workspace $\boldsymbol{P} = [x, y, z]^T$ is a collection of the position of the robot tip in the base coordinate system O_{1b} (x_{1b}, y_{1b}, z_{1b}), which is an important criterion to evaluate the manipulation area of the robot.

2) Configuration space $\boldsymbol{\Psi} = [\theta_m, \delta_m]^T$ (m = 1, 2) includes the bending angle and the rotation angle of joint m, which are named θ_m and δ_m, respectively. The configuration space reflects the shape of the continuum robot.

3) Driving space $\boldsymbol{Q} = [l_{m,n}]^T$ (m = 1, 2, n = 1, 2, 3) covers the length of the whole driving wires, where $l_{m,n}$ represents the length of the n^{th} driving wire of joint m. The driving space is a direct input variable used to control the continuum robot.

2.3 Kinematic model

For a two-joint wire-driven continuum robot, as the three driving wires of joint 2 pass through joint 1, if joint 1 bends, the lengths of driving wires of joint 2 will be changed as well. Therefore, when considering the mapping relationship between the driving space $\boldsymbol{Q}$ and the configuration space $\boldsymbol{\Psi}$, the kinematic coupling of the two joints should be taken into account:

$$l_{m,n} = \sum_{k=1}^{m}[L_k - r\theta_k \cos(\delta_k + (n-1)\alpha + (m-1)\beta)] \quad (m=1,2,\ n=1,2,3) \tag{1}$$

where L_k represents the length of the joint k (i.e. the length of the backbone included in joint k), r is the radius of the distribution circle, $\alpha = 120^\circ$ indicates the angle of the three driving wires along the circumference of the distribution circle in each constraint disk, and $\beta = 60^\circ$ is the angle between the driving wires of joints 2 and 1, as shown in Fig.1.

According to Eq. (1) and the geometrics of the continuum robot, it can be found that for each given set in the configuration $\boldsymbol{\Psi}$, there exists a unique solution in the driving space $\boldsymbol{Q}$ and vice versa.

From Fig. 1, the homogeneous transformation matrix ${}^{mb}_{me}T(m=1,2)$ from the coordinate system O_{mb} to O_{me} can be expressed by Eq. (2). Therefore, the kinematic mapping relationship between the configuration space $\boldsymbol{\Psi}$ and the workspace $\boldsymbol{P}$ can be obtained as Eq. (3).

$${}^{mb}_{me}\boldsymbol{T} = Rot(z,\delta_m)\cdot Trans[\frac{L_m}{\theta_m}(1-\cos\theta_m), 0, \frac{L_m}{\theta_m}\sin\theta_m]\cdot Rot(y,\theta_m) \quad (m=1,2) \tag{2}$$

$$\boldsymbol{P} = {}^{1b}_{1e}\boldsymbol{T} \cdot Rot(z, \beta - \delta_1) \cdot {}^{2b}_{2e}\boldsymbol{T} \cdot O_{1b} \tag{3}$$

where *Rot* and *Trans* represent the rotation and translation transformation, respectively.

From Eq. (2) and (3), we can see that for each given set in the configuration $\boldsymbol{\Psi}$, there exists a unique solution in the workspace $\boldsymbol{P}$, however, there may be multiple different configurations corresponding to a certain position in the workspace $\boldsymbol{P}$.

Thus, the forward kinematics of the wire-driven continuum robot from the driving space $\boldsymbol{Q}$ to workspace $\boldsymbol{P}$ has a unique solution, while the inverse kinematics from the workspace $\boldsymbol{P}$ to driving space $\boldsymbol{Q}$ may have multiple solutions. Moreover, it's difficult to determine the explicit solution because of the complicated expression of Eq. (3), so numerical solutions are used to obtain the inverse kinematics of the continuum robot.

3. Orientability Analysis

3.1 Orientability indices

Based on the kinematic model, the orientability of the continuum robot will be discussed in this section. Abdel-Malek et al.[20] proposed the concept of accessible region for manipulators in 1994. Based on that, Badescu et al.[22] carried a further study on orientability for a multi-segmented rigid robotic arm. These efforts provide inspiration for the analysis of the orientability of the continuum robot in this paper.

From the kinematic relationships in Section 2, it can be seen that the continuum robot reaches a given manipulation area, named task space $\boldsymbol{T}$, inside its workspace with a variety of different configurations. For instance, to paint a part, the task space $\boldsymbol{T}$ can be defined as a circumscribed sphere. For the convenience of analyzing, the task space $\boldsymbol{T}$ is assumed to be centered at point *C* with a radius *R*, as shown in Fig. 2.

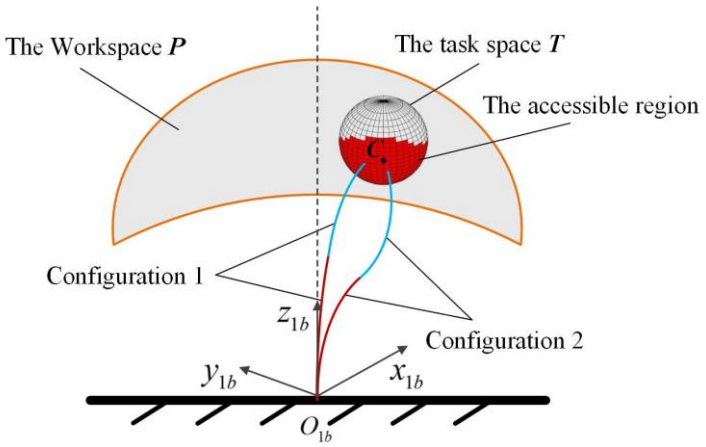

Fig. 2 The accessible region in a task space

By defining the surface area of the task space $\boldsymbol{T}$ where the robot tip can pass through with different configurations as the accessible region, the accessible ratio of the continuum robot with respect to the task space $\boldsymbol{T}$ can be expressed as

$$D(\boldsymbol{T}) = \frac{A_C}{A_T} = \frac{A_C}{4\pi R^2} \quad D(\boldsymbol{T}) \in [0,1] \tag{4}$$

where A_C represents the area of the accessible region, A_T represents the surface area of the task space $\boldsymbol{T}$.

For the surface of the task space $\boldsymbol{T}$, if we divide it into equal-area $M \times N$ patches in terms of longitude and latitude, Eq. (4) can be simplified to

$$D(\boldsymbol{T}) = \frac{K}{M \times N} \tag{5}$$

where K indicates the number of the patches that included by the accessible region.

Eq. (5) reflects the number of orientations that the robot can hold for entering a given task space. However, in many cases, e.g. painting[26] or drilling tasks[27], it is expected that the robot tip can approach the task space as perpendicular as possible to ensure enough contact in the normal direction for better operational performance. As shown in Fig. 3, assuming the robot intersects with a certain patch on the task space at point B, the tip position of the robot is point A, the center of the patch is point D, and the center of the task space $\boldsymbol{T}$ is point C. Then, the angle between the vectors $\overrightarrow{AB}$ and $\overrightarrow{CD}$ is defined as the accessible angle ω expressed by

$$\omega = \arccos \frac{\overrightarrow{AB} \cdot \overrightarrow{CD}}{|\overrightarrow{AB}| \cdot |\overrightarrow{CD}|} \quad \omega \in [0, 90°] \tag{6}$$

Assume the tip part of the continuum robot inside the task space $\boldsymbol{T}$ is relatively small in comparison to the whole joint lengths of the robot, so the vector $\overrightarrow{AB}$ can approximate the tangent line of the robot at point B. The accessible angle ω will then reflect the perpendicularity of the robot tip pointing to the accessible region on the surface of the task space $\boldsymbol{T}$.

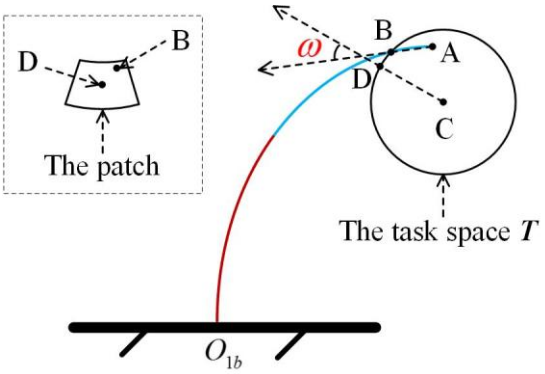

Fig.3 The accessible angle ω

For different configurations passing through the same patch in the accessible region, the value of their accessible angle ω are different. To ensure the operational performance, it is desirable to use the configuration with the minimum accessible angle ω, denoted as $\omega_{\min}$, for this patch. Thereby, the average of the minimum accessible angle $\omega_{\min}$ in the entire accessible region with respect to the task space $\boldsymbol{T}$ can be calculated by

$$\Omega(\boldsymbol{T}) = \frac{\sum_{i=1}^{K} \omega_{\min i}}{K} \tag{7}$$

In this paper, the orientability in the task space $\boldsymbol{T}$ will be comprehensively reflected by the above two indices: the accessible ratio $D(\boldsymbol{T})$ and the average minimum accessible angle $\Omega(\boldsymbol{T})$. The larger the value of $D(\boldsymbol{T})$ and the smaller the value of $\Omega(\boldsymbol{T})$ are, the better orientability performance the robot will achieve.

3.2 The analysis of orientability in the task space $\boldsymbol{T}$

Orientability in the task space $\boldsymbol{T}$ is obtained through the following steps:

1) Determine the location of the task space $\boldsymbol{T}$ and divide its surface into equal-area $M \times N$ patches in terms of longitude and latitude.

2) Generate random samples with Monte-Carlo method in the configuration space $\boldsymbol{\Psi}$ and use the forward kinematics to find the corresponding robot tip positions that can enter the task space $\boldsymbol{T}$.

3) Search the intersection of the robot and the surface of the task space $\boldsymbol{T}$ and record the position of the patch where the intersection occurs.

4) Use Eq. (5) and (7) to calculate the value of $D(\boldsymbol{T})$ and $\Omega(\boldsymbol{T})$.

Large orientability means a large bending level of the continuum robot, which is relevant to the following parameters: the individual joint length L_m (m = 1,2, L_m also

indicates the initial length of the driving wires in joint m), the length changes of the driving wires $\Delta l_{m,n} = L_m - l_{m,n}$ (m = 1,2, n = 1,2,3), and the radius of the driving wires distribution circle r. According to the geometric model shown Fig. (1) and Eq. (1), it can be found that in a bending plane, increasing the value of $\Delta l_{m,n}$ while decreasing the value of r will result in larger bending angle θ_m (m = 1, 2), i.e., $\Delta l_{m,n} = r\theta_m$. And larger bending angle θ_m allows for better dexterity and orientability[16, 24]. However, the influence of L_m on the orientability is not straightforward. Thus, this paper discusses the orientability with respect to the individual joint length L_m while assuming other parameters are given.

Below is an example showing the orientability of the robot in a task space $\boldsymbol{T}$ with different joint length combinations. Suppose the point C = (250mm, 200mm, 700mm) and R = 50mm are the center and radius of the spherical task space $\boldsymbol{T}$, respectively. The number of the patches on the surface of the task space $\boldsymbol{T}$ is set to 800, that is, M = 40 and N = 20. Three combinations of the joint lengths are assigned as (L_1 = 550mm, L_2 = 220mm), (L_1 = 600mm, L_2 = 220mm), and (L_1 = 550mm, L_2 = 240mm). 10 million random samples in the configuration space $\boldsymbol{\Psi}$ are then used to calculate orientability via Monte-Carlo method.

Figure 4 plots the accessible regions and minimum accessible angles obtained from the three joint length combinations. In each case, the results are shown in two view directions, the front and back view of the spherical task space $\boldsymbol{T}$. The accessible region is represented by colored patches. The darker patches indicate the smaller value of the minimum accessible angle $\omega_{\min}$, which is better for manipulation, and vice versa.

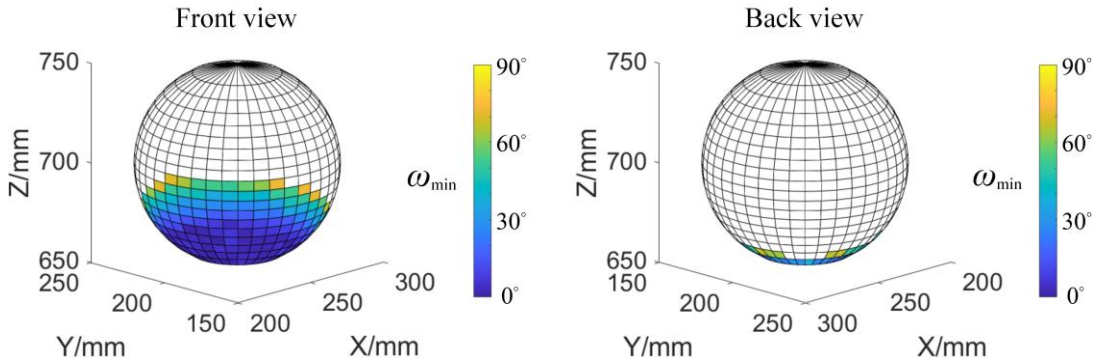

(a)

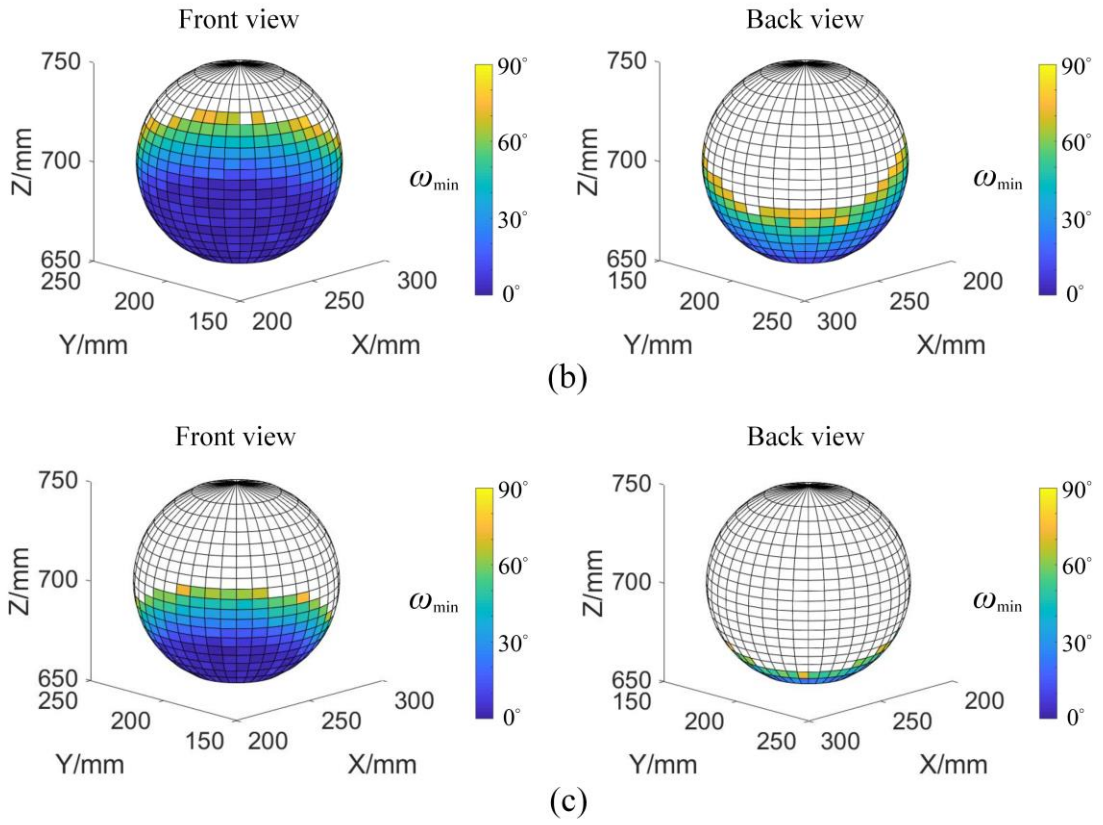

Fig. 4 The orientability description in the task space $\boldsymbol{T}$ with different joint length combinations (each subfigure has two perspectives): (a) (L_1 = 550mm, L_2 = 220mm), number of the colored patches: 244, $D_1(\boldsymbol{T})$ = 0.31, $\Omega_1(\boldsymbol{T})$ = 20.81°; (b) (L_1 = 600mm, L_2 = 220mm), number of the colored patches: 501, $D_2(\boldsymbol{T})$ = 0.63, $\Omega_2(\boldsymbol{T})$ = 23.38°; (c) (L_1 = 550mm, L_2 = 240mm), number of the colored patches: 256, $D_3(\boldsymbol{T})$ = 0.33, $\Omega_3(\boldsymbol{T})$ = 24.52°.

From Fig. 4 (a), (b) and (c), it can be seen that different joint length combinations result in large differences in the accessible ratio $D(\boldsymbol{T})$ and the average minimum accessible angle $\Omega(\boldsymbol{T})$. Comparing (a) with (b), if L_1 increases by 50mm and L_2 remains constant, $D(\boldsymbol{T})$ will increase by 103.23%. Comparing (a) with (c), if L_2 increases by 20mm and L_1 remains constant, $\Omega(\boldsymbol{T})$ will increase by 17.83%. It is found that $D(\boldsymbol{T})$ and $\Omega(\boldsymbol{T})$ is mainly affected by L_1 and L_2, respectively. Therefore, it is necessary to determine the optimal length for each joint in a continuum robot to meet the need for both indices of $D(\boldsymbol{T})$ and $\Omega(\boldsymbol{T})$, and ensure the orientability in a given task space.

4. Structural Optimization

4.1 Problem statement

To obtain the optimal individual joint lengths with respect to the orientability indices, i.e. the accessible ratio $D(\boldsymbol{T})$ and the average minimum accessible angle $\Omega(\boldsymbol{T})$, in a given task space $\boldsymbol{T}$, the problem can be stated as follows.

$$\begin{aligned} &\max F = \lambda_1 \cdot D(\boldsymbol{T}) + \lambda_2 \cdot [1 - \Omega(\boldsymbol{T}) / 90^\circ] \\ &s.t. \begin{cases} \lambda_1 + \lambda_2 = 1 \ \ (\lambda_1, \lambda_2 \in [0,1]) \\ L_1 \geq a, L_2 \geq a \\ b \leq L_1 + L_2 \leq c \end{cases} \end{aligned} \tag{8}$$

where $D(\boldsymbol{T}) = f(L_1, L_2)$, $\Omega(\boldsymbol{T}) = g(L_1, L_2)$, f and g are the forward kinematics of the continuum robot, λ_1 and λ_2 are the weights of the indices $D(\boldsymbol{T})$ and $\Omega(\boldsymbol{T})$, respectively. a is the minimum value of the individual joint lengths, b and c are the minimum and maximum value of the total length, respectively. Note that, it is difficult to obtain the explicit expressions of the functions f and g due to the highly complicated and nonlinear kinematic relationships. Thus, the calculation of F is based on a Monte-Carlo method described in Section 3.2. The selection of a, b and c depends on the practical task, for instance, the distance between the robot base and the center of the task space, and the engineering limitations of the actuators, transmissions and structural stiffness.

4.2 PSO optimization

In this section, we use the example given in Section 3.2 to demonstrate the optimization process. The task space $\boldsymbol{T}$ is a sphere with a radius of 50mm centered at C = (250mm, 200mm, 700mm). The distance between the robot base and the centroid C is 769.7mm, thus, the total length $L = L_1 + L_2$ of two joints should be greater than 769.7mm (i.e. b = 769.7mm). On the other hand, too large L will lead to issues on structural stiffness and control precision, so we limit the total length L to be less than 1000mm (i.e. c = 1000mm). In the meantime, to guarantee the robot body contains the necessary backbone, driving wires and constraint disks. The minimum length of each joint is set to 200mm (i.e. a = 200mm) and the radius of the driving wire distribution circle is 15mm (i.e. r = 15mm). The values of L_1 and L_2 are then optimized by using an improved PSO algorithm[28] based on decomposition principle. During the optimization process, the objective space is decomposed into a set of sub-regions based on a set of direction vectors, and the local optimal solutions are searched separately between the regions. Then, the crowding distance is utilized to calculate the fitness values of the reserved solutions and determine the global optimal solution.

PSO algorithm can deal with optimal problems whose objective function is implicit, so it is employed in our study. The population size, the maximum number of iterations, the learning factors and the inertia weight of the improved PSO are assigned as $N = 30$, $T = 80$, $C_1 = C_2 = 1.4962$ and $\rho = 0.7298$, respectively.

To compare the influence of the weights for the indices $D(\boldsymbol{T})$ and $\Omega(\boldsymbol{T})$, three case studies are carried out where the weights λ_1 and λ_2 have different values as shown in Table I. It was found that in Table I, although the maximum of F in the three cases are similar, the corresponding joint lengths are quite different. Increasing weight λ_1 will result in an increase of joint length L_1 and decrease of joint length L_2, and vice versa. This is consistent to the results shown in Fig. 4 that different joint lengths L_1 and L_2 have significant impacts on the value of $D(\boldsymbol{T})$ and $\Omega(\boldsymbol{T})$. Note that, in practical design of robots, the weights λ_1 and λ_2 are usually pre-determined according to the task requirements (e.g., requiring the robot to access more region or to access a region with more minimum angles). So, in our study, we don't focus on comparing the maximum of $D(\boldsymbol{T})$, $\Omega(\boldsymbol{T})$ and F by changing the weights λ_1 and λ_2. Instead, we focus on investigating the impacts of joint lengths L_1 and L_2 on the value of $D(\boldsymbol{T})$, $\Omega(\boldsymbol{T})$ and F with respect to given cases of weights λ_1 and λ_2.

The improved PSO evolution curve of the objective function F is shown in Fig.5. It can be seen that, in each case, the evolution of joint lengths L_1 and L_2 will significantly change the value of F and the maximum value of F can be obtained after about 50 iterations.

Table I. The results of the improved PSO optimization

Case	(λ_1, λ_2)	(L_1, L_2)/mm	$D(\boldsymbol{T})$	$\Omega(\boldsymbol{T})/^\circ$	F
1	(0.5,0.5)	(590,250)	0.71	23.06	0.73
2	(0.9,0.1)	(610,230)	0.72	26.24	0.72
3	(0.1,0.9)	(560,270)	0.68	21.92	0.75

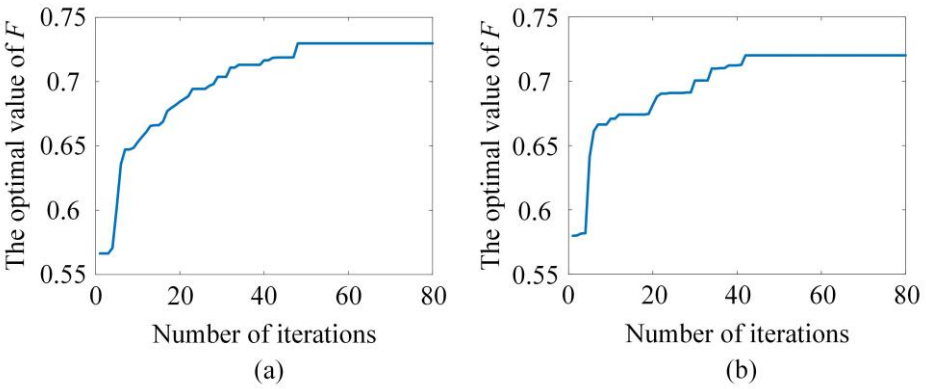

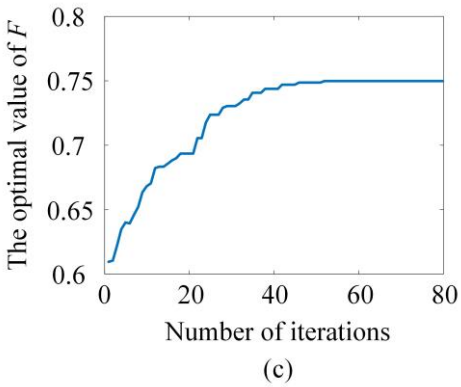

Fig. 5 The improved PSO evolution curve of the optimal orientability value of F: (a) Case 1: $\lambda_1 = 0.5$, $\lambda_2 = 0.5$; (b) Case 2: $\lambda_1 = 0.9$, $\lambda_2 = 0.1$; (c) Case 3: $\lambda_1 = 0.1$, $\lambda_2 = 0.9$.

The corresponding accessible regions and minimum accessible angles in the three cases are presented in Fig. 6. It can be seen that, when the weight of $D(\boldsymbol{T})$ gets larger, the area of the accessible region expands (i.e. the number of the colored patches increases), which is consistent with the results given in Table 1. In the accessible region, the color of the patches gets brighter, indicating the index $\Omega(\boldsymbol{T})$ and manipulation performance get worse.

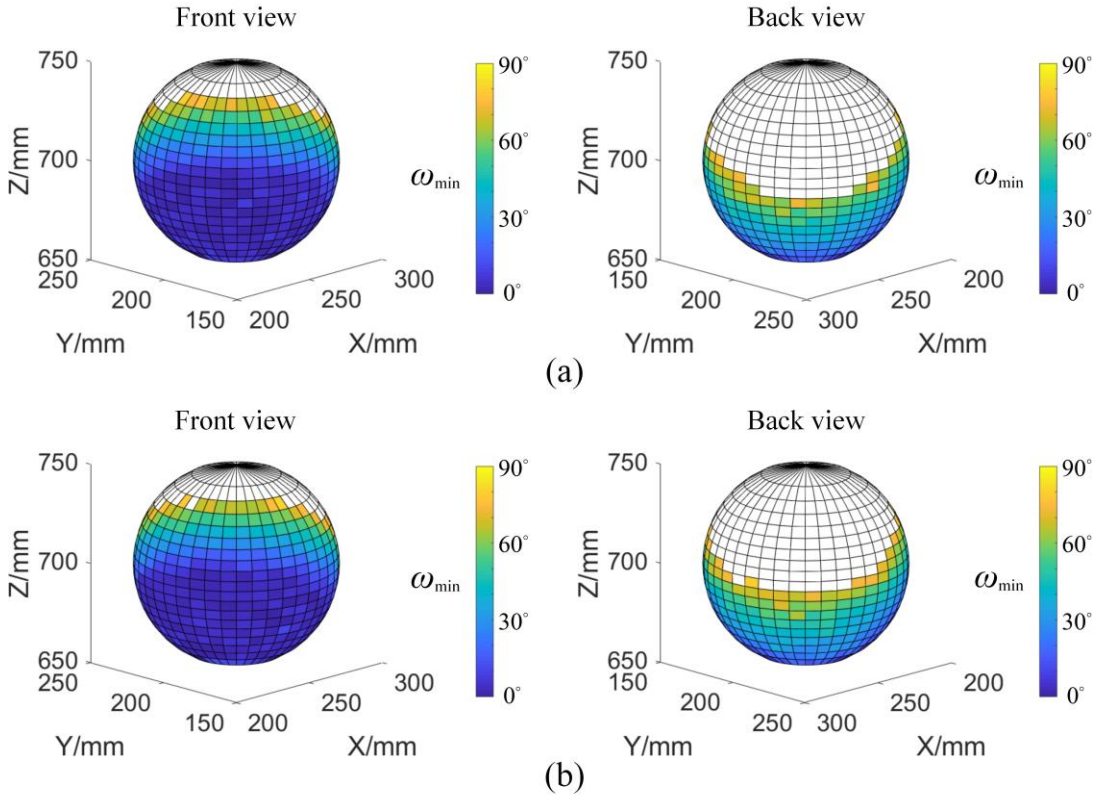

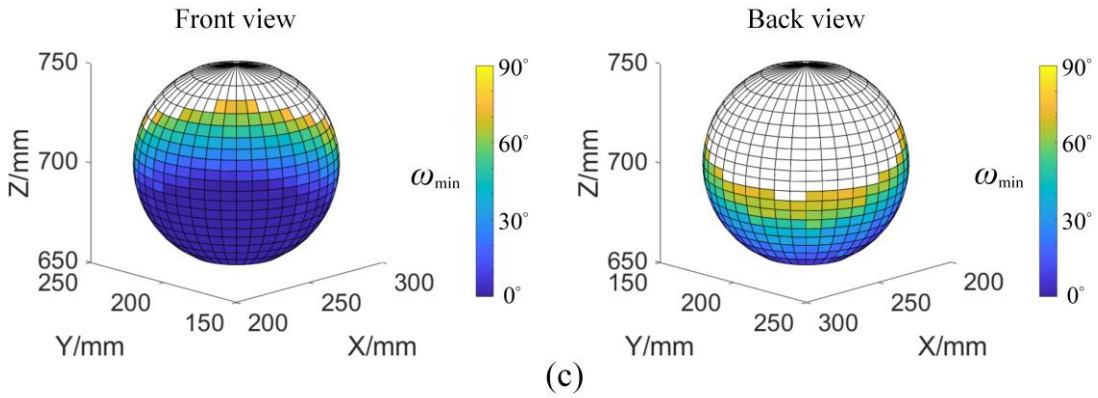

(c)

Fig. 6 The optimal orientability distribution in three cases: (a) Case 1: λ_1 = 0.5, λ_2 = 0.5, number of the colored patches: 568; (b) Case 2: λ_1 = 0.9, λ_2 = 0.1, number of the colored patches: 576; (c) Case 3: λ_1 = 0.1, λ_2 = 0.9, number of the colored patches: 544.

4.3 Results validation

In this section, a case study using traditional Monte-Carlo searching method is introduced to demonstrate the impact of joint length and to validate the PSO algorithm. The searching space is defined within 200mm ≤ L_1 ≤ 800mm, 200mm ≤ L_2 ≤ 800mm, and the weights are assigned as λ_1 = λ_2 = 0.5. It is found that the results obtained by the improved PSO algorithm are consistent with the Monte-Carlo method, as shown in Fig.7. By repeating the optimization with the improved PSO algorithm for several times, the results always converge to the global optimal solution F = 0.73 when L_1 = 590mm and L_2 = 250mm. So, the improved PSO is a feasible method for the optimization problem in this paper.

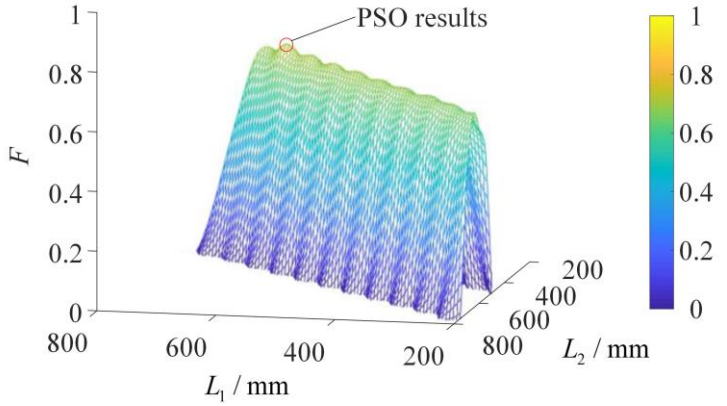

Fig. 7 Results comparison of the improved PSO algorithm and Monte-Carlo method

5. Experimental Verification

In this section, a two-joint wire-driven continuum robot is constructed to carry out the experimental verification. Assuming that we expect a continuum robot to have

balanced performance between the accessible ratio $D(\boldsymbol{T})$ and average minimum accessible angle $\Omega(\boldsymbol{T})$ in normal operations, the joint lengths L_1 = 590mm and L_2 = 250mm shown in Table 1 (case 1) is chosen for the robotic prototype to demonstrate the effects of optimization. Also, we modify the prototype to a traditional structure using equal joint length, $L_1 = L_2$ = 420mm, to compare with the optimized one.

Figure 8 shows the experimental platform including a continuum robotic prototype and a 3D electromagnetic tracking system (3D Guidance trakSTAR produced by NDI, measure error: below 0.5mm). The motion of the continuum robot is achieved through kinematic control. Given a desired configuration $[\theta_m, \delta_m]$, the controller will calculate the corresponding displacement $\Delta l_{m,n}$ for the driving wires through the inverse kinematic model, and then activate the motor and screw system to push or pull the driving wires. The electromagnetic tracking system then provides feedback on the position information along the robot by placing a sensor probe on desired points.

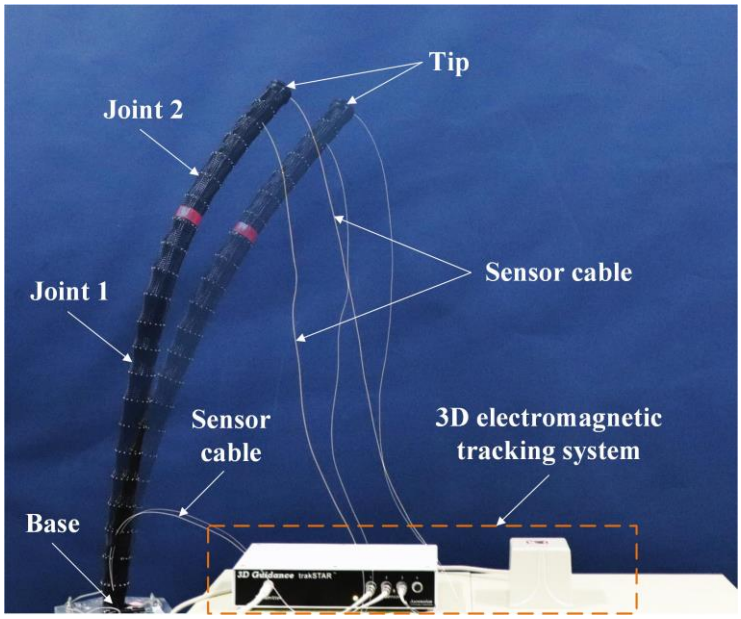

Fig. 8 The experimental platform

It can be seen from Fig.6 (a) that the distribution of the accessible region is symmetrical, so 30 patches are taken and classified into three groups G_1, G_2 and G_3 whose minimum accessible angles $\omega_{\min}$ are within [0, 30°], [30°, 60°] and [60°, 90°], respectively. For each patch, the simulated configuration with minimum accessible angle can be obtained by using Eq. (6), then the obtained configuration is used as an input to the robotic prototype to perform the experiment on orientability. Figure 9 shows a schematic diagram of how to determine the intersecting patch and the value of $\omega_{\min}$ in the experiments. The position sensor probe detects four reference points on the robot body with a distance of 25mm, 50mm, 75mm and 100mm from the robot tip. Then, the actual configuration of the robot's end part can be obtained by using the least squares based fitting method with respect to the four reference points. Finally,

the intersection of the robot and patch, as well as the value of the minimum accessible angle ω_{min} can be calculated using Eq. (6).

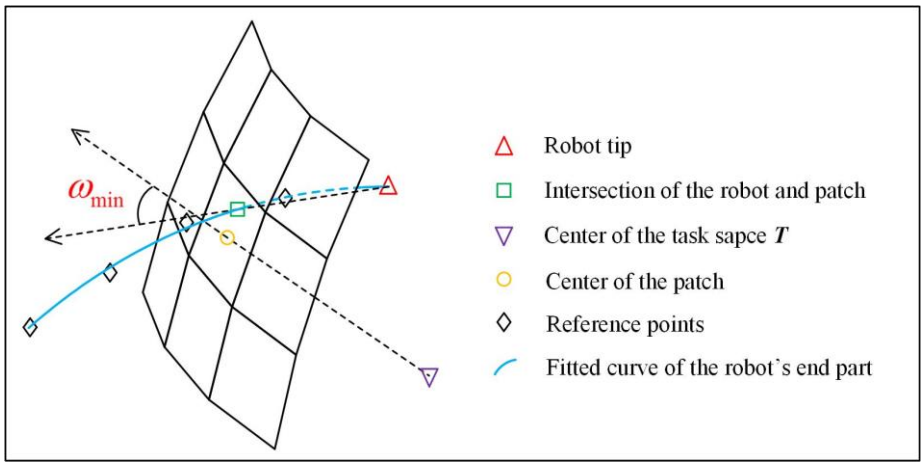

Fig. 9 The schematic diagram of the experimental process

The experimental and simulated results of the optimal joint length (L_1 = 590mm, L_2 = 250mm) are shown in Fig. 10 (a) and (b). It can be seen that the distribution of the patches are consistent, however, it is difficult to tell the color difference for each patch, which represents the value of the minimum accessible angle ω_{min}. Figure 11 gives a more detailed comparison showing the values of ω_{min} in different groups. Each triangle or circle represents the value of ω_{min} corresponding to a patch. The root mean square errors (RSME) are then calculated based on these ω_{min} values for groups G_1, G_2 and G_3, which are 2.51°, 1.89° and 2.23°, respectively. Errors are mainly due to the gap between the theoretical kinematic model and the robotic prototype, such as the friction that is not considered in the kinematic model. Also, the measurement systems and curve fitting process will introduce minor errors.

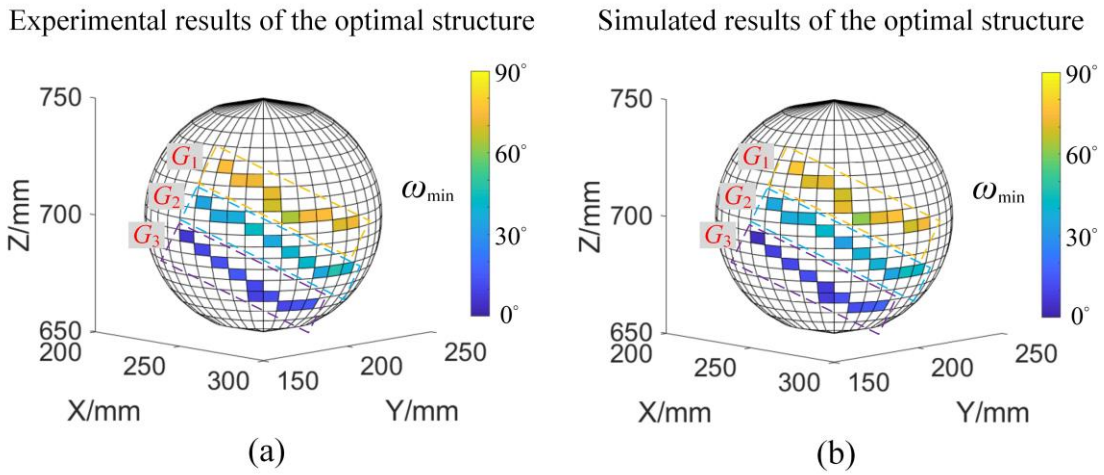

Fig. 10 Comparison between experimental and simulated results for the optimal joint length (L_1 = 590mm, L_2 = 250mm): (a) experimental results; (b) simulated results.

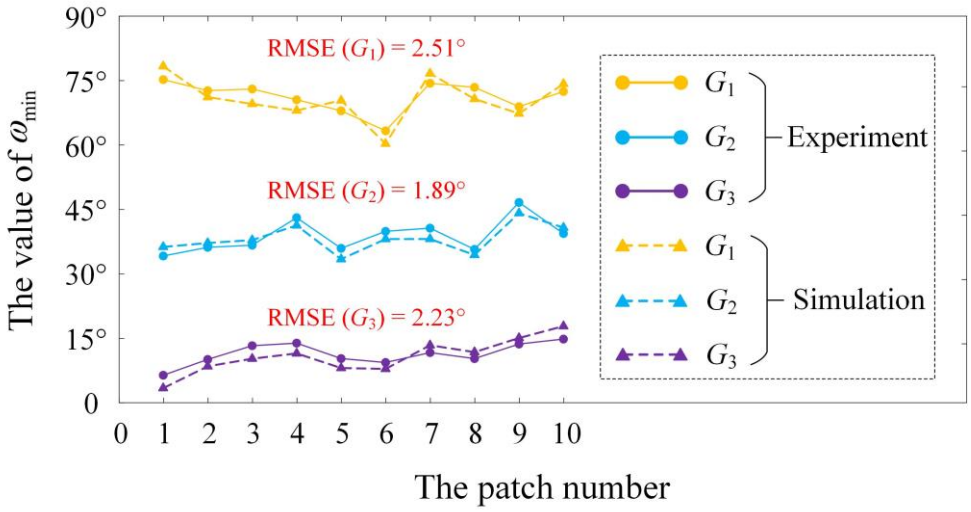

Fig. 11 Comparison of experimental and simulated results of ω_{min} with the optimal joint length (L_1 = 590mm, L_2 = 250mm)

By maintaining the total length of the robotic prototype while changing the joint length to L_1 = L_2 = 420mm, the experimental results are presented in Fig. 12. Three groups of patches G_4, G_5 and G_6 are selected in the areas where the minimum accessible angles ω_{min} are within [0, 30°], [30°, 60°] and [60°, 90°], respectively, corresponding to that for G_1, G_2 and G_3.

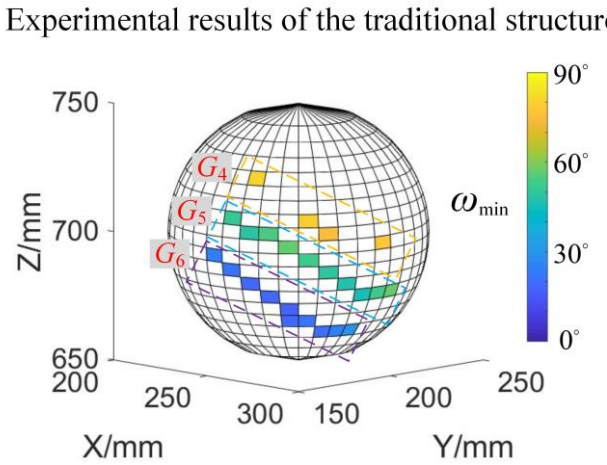

Fig. 12 Experimental results for the traditional equal joint length (L_1 = L_2 = 420mm)

Comparing Fig. 10 (a) with Fig. 12 in terms of the accessible ratio $D(\boldsymbol{T})$ index, it is found that the prototype using optimal joint length (L_1 = 590mm, L_2 = 250mm) has 10 patches in G_1 while its counterpart using equal joint length (L_1 = L_2 = 420mm) has only 4 patches in G_4. This means that the optimal joint length can achieve larger accessible region than the traditional one. For the minimum accessible angle ω_{min}, Fig. 13 gives a detailed comparison between the prototypes using optimal and equal joint lengths. As G_4 contains only 4 patches, RMSE (G_1, G_4) is calculated based on these four patches (i.e. patches 1,5,6,9 in Fig. 13). However, RMSE (G_2, G_5) and

RMSE (G_3, G_6) are calculated based on 10 patches (i.e. patches 1, 2, … ,10 in Fig. 13). It can be seen that the use of optimal joint length reduces the minimum accessible angle by more than 10° in all cases, which means a better orientability with respect to the index $\Omega(\boldsymbol{T})$.

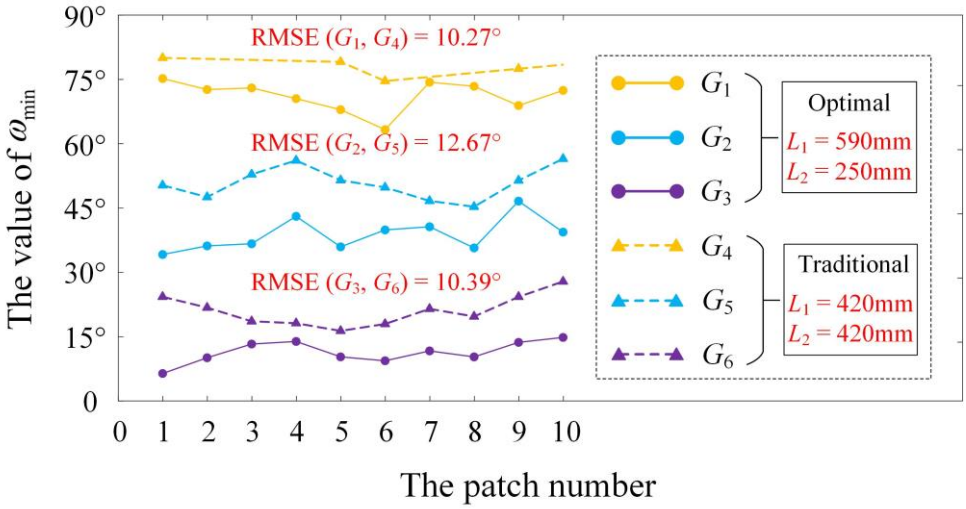

Fig. 13 Comparison of experimental results of ω_{min} between the optimal joint length and traditional equal joint length

6. Conclusions

In this paper, the orientability of a wire-driven continuum robot in a task space was defined and analyzed in detail based on a kinematic model. It was evaluated by two indices: the accessible ratio and the average minimum accessible angle, which reflected the size of the accessible region and the perpendicularity of the robot tip pointing to the task surface, respectively. The optimal joint lengths of the robot were then obtained to improve the orientability by using an improved PSO method. It was found that increasing the length of the proximal joint will enlarge the accessible ratio while increasing the length of the distal joint will reduce the minimum accessible angle. Finally, a prototype of the continuum robot was constructed to validate the presented methods. The experimental results show that using optimized unequal joint length instead of traditional equal joint length can increase the accessible region and reduce the minimum accessible angle by more than 10°. This work gives a new insight into the determination of design qualities affecting dexterity of continuum robots, and provides a foundation for further investigation into the design of multi-joint continuum robots. Future work will improve the two-joint continuum robot to a multi-joint one and use the presented methods to optimize its orientability. The orientability indices will be utilized to guide the path planning[29] and kinematic control of the multi-joint continuum robot, so that the robot can adjust its configuration to avoid obstacles while maintaining optimal orientability to a specific task space.

Declaration of Conflicting Interests

The author(s) declared no potential conflicts of interest with respect to the research, authorship, and/or publication of this article.

Funding

The author(s) disclosed receipt of the following financial support for the research, authorship, and/or publication of this article: The authors are grateful for the financial support from the National Key R&D Program of China (Grant No. 2018YFB1304600), the Natural Science Foundation of China (Grant No. 51875393, No.51605329, and No. 51721003), and the International Collaboration Programme No. B16034.

References

1. Burgner-Kahrs J, Rucker D, Choset H, Continuum robots for medical applications: A survey. IEEE Transactions on Robotics, 2015. **31**(6): p. 1261-1280.
2. McMahan W, Jones B, Walker I, Design and implementation of a multi-section continuum robot: Air-Octor, in IEEE/RSJ International Conference on Intelligent Robots and Systems (IROS). 2005. p. 2578-2585.
3. Walker I, Hannan M, A novel'elephant's trunk'robot, in IEEE/ASME International Conference on Advanced Intelligent Mechatronics. 1999. p. 410-415.
4. Hannan M, Walker I, The 'elephant trunk' manipulator, design and implementation, in IEEE/ASME International Conference on Advanced Intelligent Mechatronics. 2001. p. 14-19.
5. Simaan N, Xu K, Wei W, Kapoor A, Kazanzides P, Taylor R, Flint P, Design and integration of a telerobotic system for minimally invasive surgery of the throat. The International Journal of Robotics Research, 2009. **28**(9): p. 1134-1153.
6. Morimoto T, Okamura A, Design of 3-D printed concentric tube robots. IEEE Transactions on Robotics, 2016. **32**(6): p. 1419-1430.

7. Li M, Kang R, Branson D T, Dai J S, Model-free control for continuum robots based on an adaptive kalman filter. IEEE/ASME Transactions on Mechatronics, 2018. **23**(1): p. 286-297.
8. Kang R, Branson D, Zheng T, Guglielmino E, Caldwell D, Design, modeling and control of a pneumatically actuated manipulator inspired by biological continuum structures. Bioinspiration & biomimetics, 2013. **8**(3): p. 36008-36021.
9. Li M, Kang R, Geng S, Guglielmino E, Design and control of a tendon-driven continuum robot. Transactions of the Institute of Measurement and Control, 2018. **40**(11): p. 3263-3272.
10. Kim Y and Desai J, Design and kinematic analysis of a neurosurgical spring-based continuum robot using SMA spring actuators, in IEEE/RSJ International Conference on Intelligent Robots and Systems (IROS). 2015. p. 1428-1433.
11. Jones B and Walker I, Kinematics for multisection continuum robots. IEEE Transactions on Robotics, 2006. **22**(1): p. 43-55.
12. Camarillo D, Milne C, Carlson C, Zinn M, Salisbury J, Mechanics modeling of tendon-driven continuum manipulators. IEEE Transactions on Robotics, 2008. **24**(6): p. 1262-1273.
13. Webster III R, Romano J, Cowan N, Mechanics of precurved-tube continuum robots. IEEE Transactions on Robotics, 2009. **25**(1): p. 67-78.
14. Yuan H, Li Z, Workspace analysis of cable-driven continuum manipulators based on static model. Robotics and Computer-Integrated Manufacturing, 2018. 49: p. 240-252.
15. Burgner-Kahrs J, Gilbert H, Granna J, Swaney P, Webster R, Workspace characterization for concentric tube continuum robots, in IEEE/RSJ International Conference on Intelligent Robots and Systems (IROS). 2014. p. 1269-1275.
16. Cao K, Kang R, Branson D, Geng S, Song Z, Dai J, Workspace analysis of tendon-driven continuum robots based on mechanical interference identification. Journal of Mechanical Design, 2017. **139**(6): p. 062303.
17. Salisbury J, Craig J, Articulated hands: Force control and kinematic issues. The International journal of Robotics research, 1982. **1**(1): p. 4-17.

18. Gosselin C, Angeles J, A global performance index for the kinematic optimization of robotic manipulators. Journal of Mechanical Design, 1991. **113**(3): p. 220-226.

19. Zargarbashi S, Khan W, Angeles J, The Jacobian condition number as a dexterity index in 6R machining robots. Robotics and Computer-Integrated Manufacturing , 2012. **28**(6): p. 694-699.

20. Abdel-Malek K, Paul B, The dexterous solid angle for manipulators with a spherical wrist, in Proceedings of the 23rd ASME Mechanisms Conference. 1994. p. 341-350.

21. Abdel-Malek K. Dexterity of manipulator arms at an operating point, in Proceedings of the 21st ASME Advances in Design Automation. 1995. p. 781-788.

22. Badescu M, Mavroidis C, New performance indices and workspace analysis of reconfigurable hyper-redundant robotic arms. The International Journal of Robotics Research, 2004. **23**(6): p. 643-659.

23. Wang C, Yang C, Kang R, Kinematic flexibility analysis of a wire-driven continuum robot, in IEEE International Conference on Robotics and Biomimetics (ROBIO). 2018. p. 337-342.

24. Wu L, Crawford R, Roberts J, Dexterity analysis of three 6-DOF continuum robots combining concentric tube mechanisms and cable-driven mechanisms. IEEE Robotics and Automation Letters, 2017. **2**(2): p. 514-521.

25. Xu K, Simaan N, An investigation of the intrinsic force sensing capabilities of continuum robots. IEEE Transactions on Robotics, 2008. **24**(3): p. 576-587.

26. Chen R, Wang G, Zhao J, Xu J, Chen K, Fringe Pattern based plane-to-plane visual servoing for robotic spray path planning. IEEE/ASME Transactions on Mechatronics, 2018. **23**(3): p. 1083-1091.

27. Chen D, Yuan P, Wang T, Shi Z, Liu Y, Lin M, Perpendicularity adjustment end effector for aeronautical drilling robot, in IEEE/RSJ International Conference on Intelligent Robots and Systems (IROS). 2016. p. 2616-2621.

28. Dai C, Wang Y, Ye M, A new multi-objective particle swarm optimization algorithm based on decomposition. Information Sciences, 2015. 325: p. 541-557.

29. Ouyang B, Liu Y, Tam H, Sun D, Design of an interactive control system for a multisection continuum robot. IEEE/ASME Transactions on Mechatronics, 2018. **23**(5): p. 2379-2389.